





Rapid non-destructive volumetric tumor yield assessment in fresh lung core needle biopsies using polarization sensitive optical coherence tomography

SREYANKAR NANDY,^{1,2,3}  TIMOTHY L. HELLAND,^{3,4} BENJAMIN W. ROOP,¹ REBECCA A. RAPHAELY,^{1,3} AMY LY,^{2,3} MADELYN LEW,⁵ SARITA R. BERIGEI,¹ MARTIN VILLIGER,^{2,3}  ANASTASIA SOROKINA,^{6,7} MARGIT V. SZABARI,^{1,2,3} FLORIAN J. FINTELMANN,^{3,8} MELISSA J. SUTER,^{1,2,3} AND LIDA P. HARIRI^{1,2,3,4,*}

¹*Division of Pulmonary and Critical Care Medicine, Massachusetts General Hospital, Boston, MA 02110, USA*

²*Wellman Center for Photomedicine, Massachusetts General Hospital, Boston, MA 02110, USA*

³*Harvard Medical School, Boston, MA 02110, USA*

⁴*Department of Pathology, Massachusetts General Hospital, Boston, MA 02110, USA*

⁵*Department of Pathology, University of Michigan, Ann Arbor, MI 48104, USA*

⁶*Department of Pathology, University of Illinois at Chicago, Chicago, IL 60631, USA*

⁷*Department of Pathology, Research Institute of Human Morphology, Moscow 103132, Russia*

⁸*Department of Radiology, Massachusetts General Hospital, Boston, MA 02110, USA*

*lhhariri@mgh.harvard.edu

Abstract: Adequate tumor yield in core-needle biopsy (CNB) specimens is essential in lung cancer for accurate histological diagnosis, molecular testing for therapeutic decision-making, and tumor biobanking for research. Insufficient tumor sampling in CNB is common, primarily due to inadvertent sampling of tumor-associated fibrosis or atelectatic lung, leading to repeat procedures and delayed diagnosis. Currently, there is no method for rapid, non-destructive intraprocedural assessment of CNBs. Polarization-sensitive optical coherence tomography (PS-OCT) is a high-resolution, volumetric imaging technique that has the potential to meet this clinical need. PS-OCT detects endogenous tissue properties, including birefringence from collagen, and degree of polarization uniformity (DOPU) indicative of tissue depolarization. Here, PS-OCT birefringence and DOPU measurements were used to quantify the amount of tumor, fibrosis, and normal lung parenchyma in 42 fresh, intact lung CNB specimens. PS-OCT results were compared to and validated against matched histology in a blinded assessment. Linear regression analysis showed strong correlations between PS-OCT and matched histology for quantification of tumors, fibrosis, and normal lung parenchyma in CNBs. PS-OCT distinguished CNBs with low tumor content from those with higher tumor content with high sensitivity and specificity. This study demonstrates the potential of PS-OCT as a method for rapid, non-destructive, label-free intra-procedural tumor yield assessment.

© 2021 Optical Society of America under the terms of the [OSA Open Access Publishing Agreement](#)

1. Introduction

Lung cancer is the leading cause of cancer-related death worldwide [1]. Screening with low-dose computed tomography (CT) is recommended for early detection of lung nodules in high-risk patients [2]. However, biopsy is often required for ultimate diagnosis of malignancy [3]. Transthoracic and transbronchial core needle biopsy (CNB) are the primary methods to obtain tissue from lung nodules [4–6]. Obtaining adequate tumor yield on CNBs is essential for accurate histologic diagnosis and subtyping of lung carcinomas, which often requires immunohistochemical

(IHC) stains in addition to traditional hematoxylin and eosin (H&E) stained tissue sections. In the era of personalized medicine in lung carcinoma management, additional tumor content is often required for molecular testing to identify mutations and determine eligibility for targeted therapies [7–9]. Furthermore, clinical tumor biobanks of CNB specimens serve as an important resource for lung cancer research.

Unfortunately, tumor yields on CNB are often compromised by inadvertent biopsy of non-tumor elements, such as admixed tumor-associated fibrosis known to be prominent in lung carcinomas or adjacent atelectatic lung parenchyma [8–11]. When tumor yields on CNB are insufficient to meet clinical diagnostic requirements, repeat biopsy is needed, thereby delaying diagnosis and increasing risks of morbidity and mortality [9–11]. Low tumor yields also impede research reliant on clinical tumor biobanking specimens, ultimately slowing innovation and discovery in the field [10]. Protocols such as rapid onsite evaluation (ROSE) have been implemented for intraprocedural assessment of content in needle aspirate cytology. However, ROSE is limited to cytology specimens and does not allow for reliable assessment of tumor adequacy or quantity in corresponding CNB tissue samples. [12] Currently, no widely used rapid assessment methodology exists for adequacy assessment of CNB specimens. Rapid assessment using frozen section and/or touch prep analysis have been attempted, but these methods are destructive and consume tissue, thereby reducing the overall tumor sample available for pathologic analysis and molecular testing. Other studies have assessed confocal, fluorescent, and light sheet microscopy for non-destructive assessment of biopsy specimens. [13,14] However, these techniques require time and labor-intensive staining, complicated tissue clearing procedures, and/or long imaging times, which makes implementation for onsite rapid adequacy assessment challenging. Thus, there is a clear clinical need for a rapid, label-free, non-destructive, onsite method to assess the adequacy of CNB specimens.

Optical coherence tomography (OCT) is a label-free, non-destructive imaging modality with high resolution ($< 10 \mu\text{m}$) that provides volumetric, microscopic assessment of fresh, intact tissue specimens within seconds [15–21]. Polarization sensitive optical coherence tomography (PS-OCT) is an extension of conventional OCT that simultaneously obtains structural OCT images while detecting intrinsic optical tissue properties, such as birefringence and degree of polarization uniformity (DOPU) [22,23]. Birefringence provides intrinsic contrast to collagen, which is present in fibrosis. Previous qualitative studies of PS-OCT, including in lung and breast carcinoma, have demonstrated that collagen-rich fibrotic stroma exhibit high birefringence while tumor regions lack substantial birefringence signal [24–26]. A recent study from our group demonstrated that PS-OCT birefringence could accurately quantify fibrosis and distinguish regions of low and high fibrosis in surgical resections of primary lung carcinomas [25]. Although birefringence measurements can identify and quantify tumor-associated fibrosis as a means to potentially reduce contamination in biopsy specimens, it does not provide a direct assessment of tumor yield.

In addition to tissue birefringence, PS-OCT can also provide contrast related to the depolarization of the detected light through the degree of polarization uniformity (DOPU). Depolarization of light inside the tissue is caused by the randomization and scrambling of polarization states from light-scattering tissue microstructures. DOPU has been used for assessment of various tissue types, such as lung, breast, and cervix [27–29]. A PS-OCT study on *in vivo* human lung demonstrated the application of DOPU to identify alveolar regions of normal lung, which had low DOPU values [27]. Prior studies on breast carcinoma reported that regions of tumor tissue exhibit an overall uniformity of polarization states, resulting in high DOPU [28]. Fibrotic stroma in breast and cervical tissue have been reported to demonstrate lower polarization uniformity due to scattering and significant variation in the polarization states [28,29]. We hypothesize that the combined use of PS-OCT metrics, birefringence and DOPU, may provide a robust method for label-free, non-destructive, volumetric assessment of fibrotic and tumor components in lung

biopsy specimens. In this study, we investigate the use of PS-OCT to quantify tumor yield and fibrosis content, and distinguish tumor-rich from tumor-poor lung CNB specimens, as compared to histology.

2. Methods

2.1. CNB specimens

Fresh, intact CNB specimens were obtained from excised surgical lung nodule resection specimens from patients at Massachusetts General Hospital. The study was approved by the Mass General Brigham Institutional Review Board (IRB) (protocol number: 2010-P-002214/1). The written informed consent process was waived due to the use of de-identified excess tissue in this study. CNB specimens were obtained using a semi-automatic 20-gauge x 10 cm disposable core biopsy instrument (Bard Mission, Tempe, AZ) and matching 19-gauge introducer needle. Fresh specimens were immediately imaged with benchtop PS-OCT in a thin layer of phosphate buffered saline solution to prevent tissue drying. An ink mark was placed on one side of the biopsy specimen for precise registration between PS-OCT imaging and histology, as previously described [30].

2.2. PS-OCT imaging and processing

The details of the benchtop PS-OCT system used in this study have been previously described [25,30–31]. Briefly, the OCT imaging system consists of a fiber-based swept source with a central wavelength of 1310 nm, bandwidth of 110 nm and an A-line acquisition rate of 66 KHz. The axial and lateral resolution of the OCT system is ~ 7 and $20\text{ }\mu\text{m}$, respectively. The sample arm of the benchtop PS-OCT system consisted of a telecentric objective lens with an effective focal length of 36 mm and field of view of $9.4 \times 9.4\text{ mm}^2$ (LSM03, Thorlabs, Inc., Newton, NJ). Lateral and transverse scanning was performed with galvanometric scanners, as described in previous studies [25,30]. Cross-sectional OCT images were acquired along the long axis of each CNB specimen (2048 A-lines per image). A total of 128 cross-sectional images were acquired to achieve volumetric imaging over the 1 mm thickness of each CNB specimen (image-to-image spacing: $7.8\text{ }\mu\text{m}$). This imaging field of view of $1\text{ cm} \times 1\text{ mm}$ was chosen because CNB specimens are typically less than 1 cm in length and 1 mm in diameter. Structural and PS-OCT data were obtained simultaneously. The acquisition time for each volumetric image dataset was ~ 4 seconds. Polarization sensitivity was achieved by modulating the polarization state of the light source in successive axial depth profiles, or A-lines, between states perpendicular to each other in Stokes space, and then combining A-line pairs using Stokes vector analysis [25,31–32].

PS-OCT images were generated offline from the raw datasets using a previously described spectral binning method to mitigate polarization mode dispersion [32]. Birefringence related to the depth-resolved local retardation was calculated from spectrally binned data using a depth offset of $\sim 24\text{ }\mu\text{m}$ in tissue, ranging from 0 degrees/ $100\text{ }\mu\text{m}$ (no birefringence) to 65 degrees/ $100\text{ }\mu\text{m}$ (high birefringence) [25,31]. DOPU was independently calculated from the spectrally binned data from the average components of the normalized Stokes vectors, ranging from 0 (completely random polarization) to 1 (uniformly preserved polarization) [32]. Processing of all structural, birefringence, and DOPU data and images was performed in MATLAB (MathWorks, Natick, Massachusetts). The overall processing time to generate volumetric datasets of structural, birefringence and DOPU images for an entire CNB specimen was ~ 4.3 minutes using a GPU PC (NVIDIA GeForce GTX 1080). Volumetric birefringence and DOPU images for each CNB specimen were rendered from the series of cross-sectional images using 3D Slicer (Version 4.10.2, www.slicer.org).

2.3. PS-OCT birefringence and DOPU analysis for tissue quantification

Birefringence and DOPU values were each analyzed on a per pixel basis for each B-scan image. Noise floor filters were applied to structural OCT images (threshold: 30 dB) based on previously published data. [25] The thresholded structural OCT image was then used to mask the corresponding PS-OCT images in order to avoid noise, and isolate signal arising from regions of tissue [25,31]. Birefringence and DOPU thresholding was then applied to distinguish and quantify tumor, fibrosis, and normal lung tissue (**Fig. 1**). For each PS-OCT cross-sectional image, the outer border of the tissue region of interest (ROI) was segmented manually, and the number of pixels in the ROI satisfying both birefringence and DOPU criteria for a particular tissue group (tumor, fibrosis, or normal lung parenchyma) were divided by the total number of pixels in the ROI to obtain the percentage amount of tumor, fibrosis, and normal lung parenchyma, respectively. [25] This analysis was repeated on all the cross-sectional images in the entire volume of each CNB specimen, and the results were subsequently averaged to obtain the percentage amount of tumor, fibrotic, and normal lung tissue within each volumetric CNB specimen.

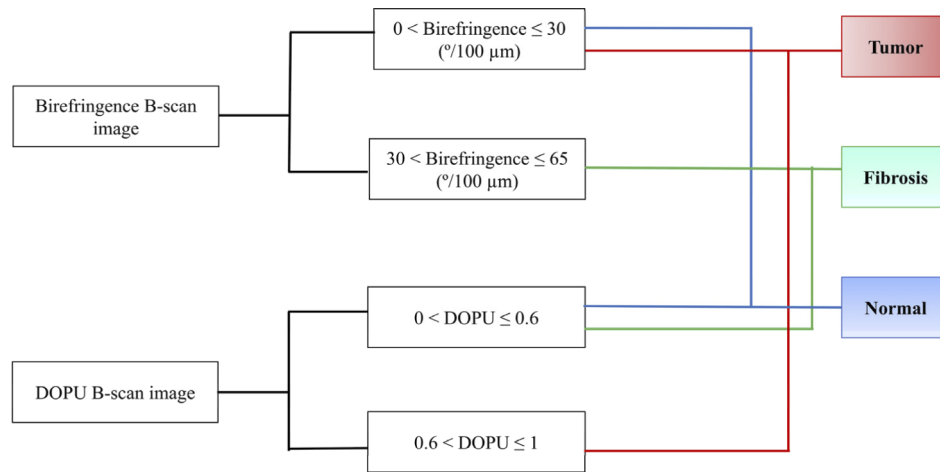


Fig. 1. PS-OCT quantification workflow.

2.4. Histopathology processing and analysis

After PS-OCT imaging, CNB specimens were fixed in 10% formalin solution for standard histopathological processing. During embedding and sectioning, each CNB was oriented to cut histologic sections along the full length of the tissue. Two serial histologic sections (5 μ m thick) were obtained from the center of each CNB specimen and stained with hematoxylin and eosin (H&E, blue: nuclei; pink: cytoplasm and extracellular matrix), and Masson's trichrome stain (blue: collagen and bone; red/pink: muscle, keratin, and cytoplasm; black: nuclei), respectively. Histology slides were digitized using a whole slide scanning system (Nanozoomer 2.0-RS, Hamamatsu). For each histologic section, the outer border of the CNB tissue area was segmented manually. An independent, board-certified pathologist manually segmented regions of tumor on digitized H&E images for each CNB. A second, independent pathologist manually segmented regions of normal lung and fibrosis on the digitized H&E and trichrome images, respectively, for each CNB. A third independent pathologist reviewed the annotated regions of tumor, normal lung, and fibrosis on the H&E and trichrome images. In cases of discordance, a consensus interpretation was determined between the pathologists, which was used as the final histologic comparator for PS-OCT. All the pathologists were blinded to PS-OCT data and analysis. For each

CNB specimen, the percentage amount of tumor, fibrosis, and normal lung were each calculated by dividing the total number of pixels in the segmented regions for each respective category by the total number of pixels in the entire CNB tissue area. Histopathology segmentation and quantification was performed using ImageJ (64-bit, version 1.52p, National Institutes of Health, Bethesda, Maryland).

2.5. Statistical analysis

Linear regression analyses were performed to individually evaluate the correlation between PS-OCT and histology for measurements of percent tumor, fibrosis, and normal lung parenchyma, respectively. Bland-Altman analysis was performed to compare the two measurement techniques for tumor, fibrosis, and normal lung quantification, respectively. The difference was calculated as the percent tissue (tumor, fibrosis, or normal lung) measured on histopathology minus the percent tissue (tumor, fibrosis, or normal lung) detected by PS-OCT for each CNB specimen, respectively. For all analyses, a P value of < 0.05 was considered statistically significant. CNB specimens with viable tumor content $\leq 25\%$ were defined as low-tumor content, while CNBs with $> 25\%$ tumor were defined as high tumor content [33]. Fisher's exact test was performed to determine the ability of PS-OCT to distinguish CNB specimens with low tumor content ($\leq 25\%$) from those with higher tumor content ($>25\%$). Similarly, Fisher's exact test was performed to determine the ability of PS-OCT to distinguish CNB specimens with low fibrosis content ($\leq 25\%$) from those with higher fibrosis content ($>25\%$). All statistical analyses were performed using R statistical software (Version 3.6.2).

3. Results

3.1. Histology

PS-OCT imaging was obtained in 47 CNB specimens from 8 patients (average: 6 CNB specimens per patient). The clinical demographics of the study cohort are presented in **Table 1**. All patients were staged as part of their clinical evaluation in accordance with the American Joint Committee on Cancer (AJCC, 8th edition) for T (size and extent of the main tumor) and N (spread to nearby lymph nodes) classification [34]. Five specimens from 3 patients were excluded from the analysis due to technical issues with PS-OCT data saving ($n=3$), loss of tissue during histology processing ($n=1$), or poor histology scan quality ($n=1$). The remaining 42 CNB specimens were included in the analysis. The dimensions of the CNB specimens ranged from 2 mm to 8 mm in length and 0.4 mm to 1 mm in thickness. On histologic analysis, 33 CNB contained some amount of tumor (mean: 10.1%, SD: 15.2%, range: 0.3%-70.6%), 42 CNB contained fibrosis (mean: 22.4%, SD: 14.4%, range: 4.3%-63.6%), and 16 CNB contained normal lung parenchyma (mean: 15.3%, SD: 28.7%, range: 4.8%-90.1%). There were no detectable tumor cells present in 9 CNB specimens, which consisted entirely of fibrosis and/or normal lung parenchyma.

3.2. Visual representations of tumor, fibrosis, and normal lung in CNB

Figures 2–5 demonstrate oblique sections from representative PS-OCT data volumes of CNB specimens where birefringence or DOPU is overlaid onto the corresponding structural OCT, and are oriented for comparison with the histopathological features. PS-OCT provides visual information about the microscopic distribution of tumor (T), fibrosis (F), and normal alveolated lung (A) within individual CNB specimens. Overall, the tumor regions demonstrate low birefringence and high DOPU signal, whereas the fibrotic regions show high birefringence and low DOPU signal (Figs. 2–4). Normal lung parenchyma (Fig. 5) shows lattice-like heterogeneous alveolar regions. Birefringence signal of low to moderate intensity is observed from collagen within the alveolar walls, as well as focal birefringence from collagen surrounding vessels. Overall, the low-signal alveoli have both low birefringence and low DOPU. Tumor associated

Table 1. Patient demographics and clinical characteristics.

Age (Mean)	72 years (range 51 - 83 years)
Sex	5 Male / 3 Female
Diagnosis	
Adenocarcinoma	30 CNB samples (5 patients)
Squamous cell carcinoma (SCC)	11 CNB samples (2 patients)
Carcinoid tumor (Typical)	6 CNB samples (1 patient)
Size of lesion (Mean)	2.8 cm (range: 1.0 - 5.5 cm)
Stage	
pT1mi	1 patient
pT1a	0 patients
pT1b	4 patients
pT1c	1 patient
pT2a	0 patients
pT2b	1 patient
pT3	1 patient
N status	
Nx	1 patient
N0	5 patients
N1a	2 patients

inflammation is often present in lung nodule biopsy specimens, frequently admixed with regions of fibrosis (**Figs. 2–4**). The presence of pigmented particles from environmental pollution or smoking, combined with inflammation may affect the regional DOPU (**Fig. 5**).

3.3. Quantification of tumor, fibrosis, and normal lung components in CNB specimens

Strong positive correlation ($r = 0.85$, $P < 0.001$) was observed between percent tumor measured on PS-OCT using the birefringence and DOPU thresholding algorithm (birefringence ≤ 30 degrees/100 μm and DOPU > 0.6) and percent tumor measured by an independent pathologist on matched histology (**Fig. 6(a)**). Bland-Altman analysis demonstrated an average bias of 5.61% overestimation by PS-OCT for tumor quantification as compared to histology (**Fig. 6(b)**). The percent fibrosis measured on PS-OCT (birefringence > 30 degrees/100 μm and DOPU ≤ 0.6) and percent fibrosis measured by an independent pathologist on matched histology also showed a strong positive correlation ($r = 0.9$, $P < 0.001$) (**Fig. 6(c)**). Bland-Altman analysis demonstrated an average bias of 4.37% underestimation by PS-OCT for fibrosis quantification as compared to histology (**Fig. 6(d)**). There was also a strong positive correlation ($r = 0.89$, $P < 0.001$) between the percent normal lung parenchyma measured on PS-OCT (birefringence ≤ 30 degrees/100 μm and DOPU ≤ 0.6) and percent normal lung parenchyma measured by an independent pathologist on matched histology (**Fig. 6(e)**). Bland-Altman analysis demonstrated an average bias of 6.58% overestimation by PS-OCT for quantification of normal lung parenchyma as compared to histology (**Fig. 6(f)**).

Fisher's exact test demonstrated that PS-OCT accurately classified CNB specimens with low-tumor content ($\leq 25\%$) from those with higher tumor content ($> 25\%$) with a sensitivity and specificity of 94.4% and 83.3%, respectively ($P < 0.0001$, **Table 2**). Similarly, Fisher's exact test demonstrated that PS-OCT accurately classified CNB specimens with low fibrosis content ($\leq 25\%$) from specimens with higher fibrosis content ($> 25\%$) with a sensitivity and specificity of 96.9% and 88.9%, respectively ($P < 0.0001$, **Table 2**).

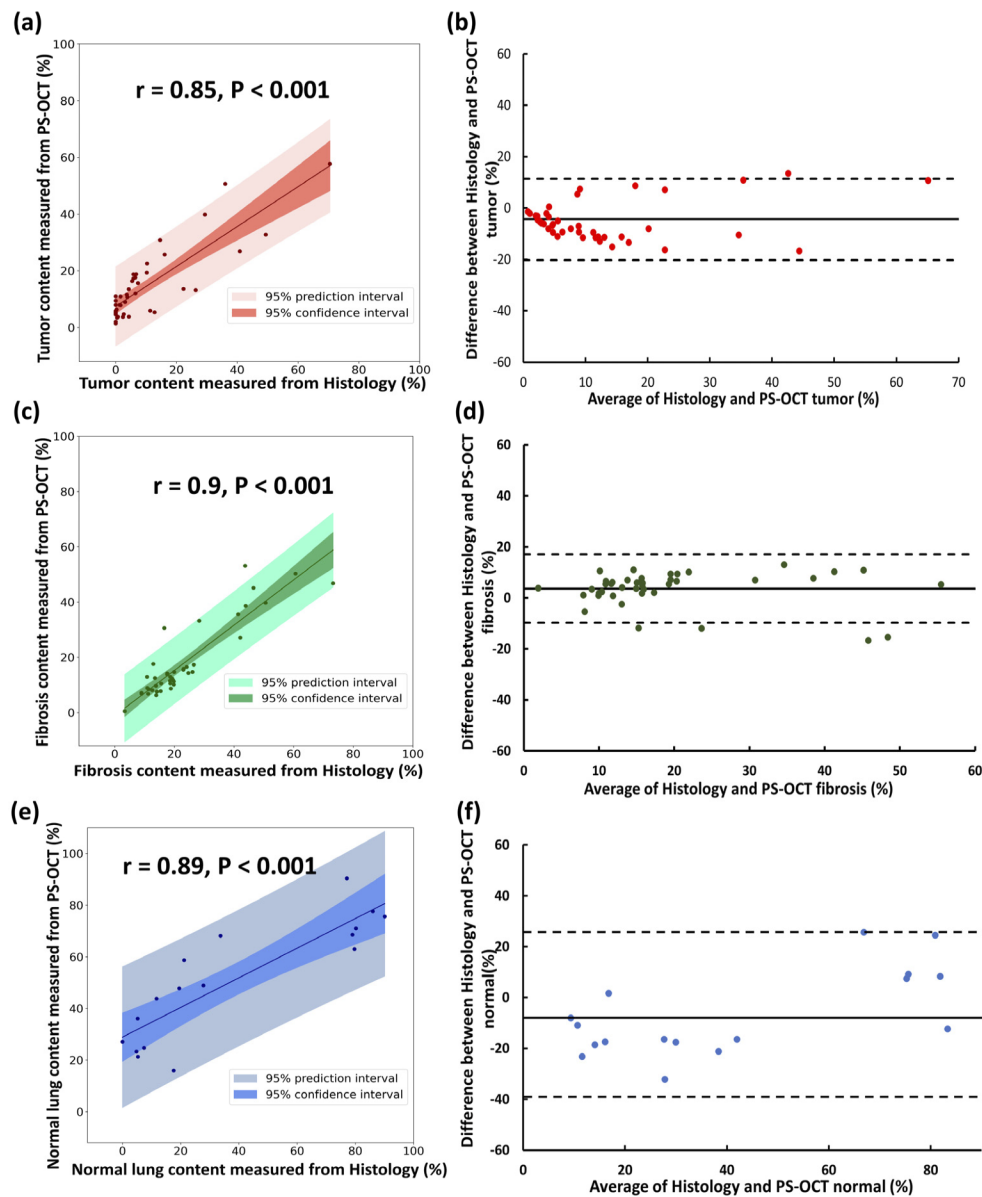


Fig. 2. Quantitative PS-OCT assessment of tumor, fibrosis, and normal lung components in CNB as compared to histology. **(a, c, e)** Linear regression analysis demonstrated strong correlation between PS-OCT and histology for quantifying **(a)** tumor ($r = 0.85$, $P < 0.001$), **(c)** fibrosis ($r = 0.9$, $P < 0.001$) and **(e)** normal lung parenchyma ($r = 0.89$, $P < 0.001$). The darker shaded bands in **(a, c, e)** indicate the 95% confidence intervals, whereas the lighter shaded bands indicate the 95% prediction intervals. **(b, d, f)** Bland-Altman analysis comparing PS-OCT and histology measurements showed an overall bias of **(b)** 5.61% for tumor, **(d)** -4.37% for fibrosis and **(f)** 6.58% for normal lung parenchyma, respectively. The dotted lines in **(b, d, f)** indicate the upper and lower 95% confidence intervals.

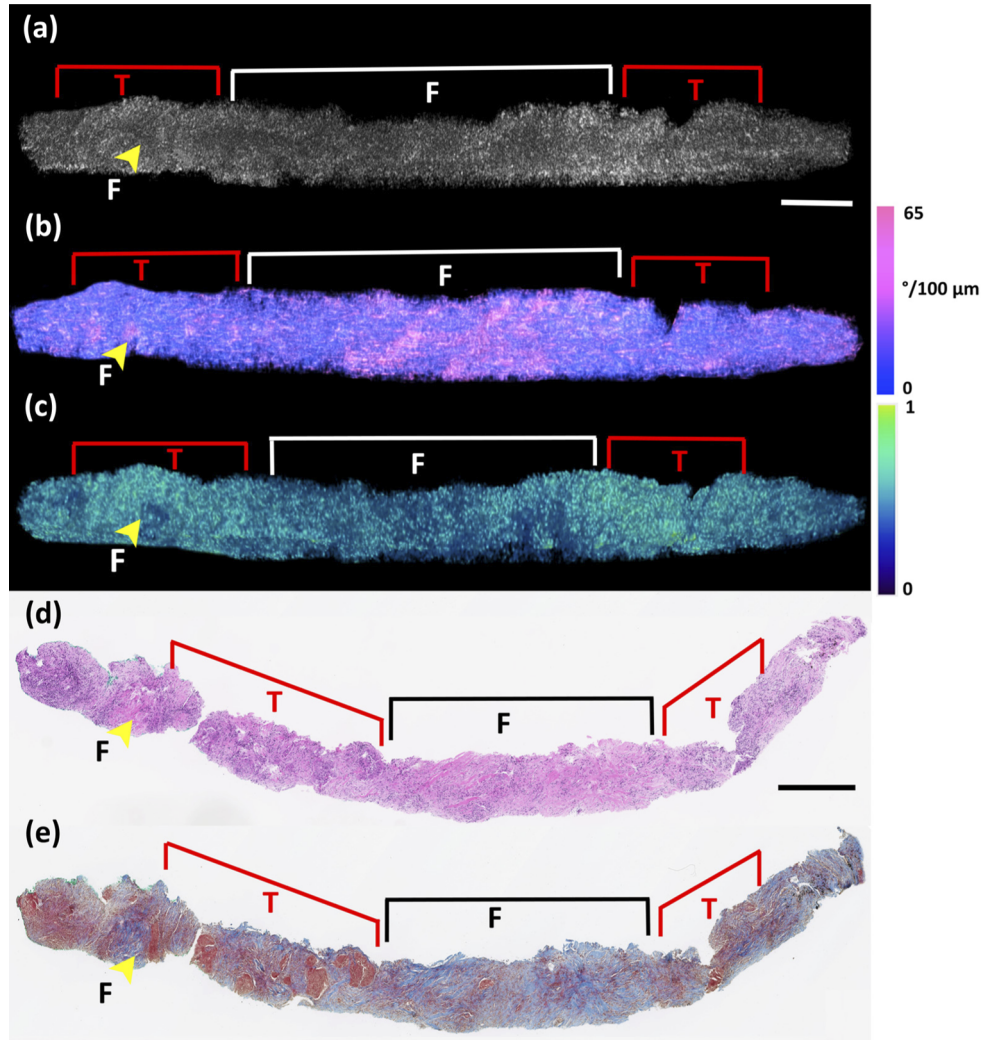


Fig. 3. Volumetric (a) structural, (b) birefringence and (c) DOPU images oriented and cut obliquely for comparison with the histopathological features in the corresponding (d) H&E and (e) trichrome sections of a CNB specimen with adenocarcinoma (T) mixed with dense fibrosis (F) and inflammation. Birefringence colormap (b, right), ranging from $0^\circ/100\ \mu\text{m}$ (no birefringence) to $65^\circ/100\ \mu\text{m}$ (high birefringence). DOPU colormap (c, right), ranging from 0 (low DOPU) to 1 (high DOPU). Corresponding (d) H&E and (e) trichrome stained histology confirms the presence of tumor and fibrosis with inflammation in the CNB specimen. Scalebars: 0.5 mm.

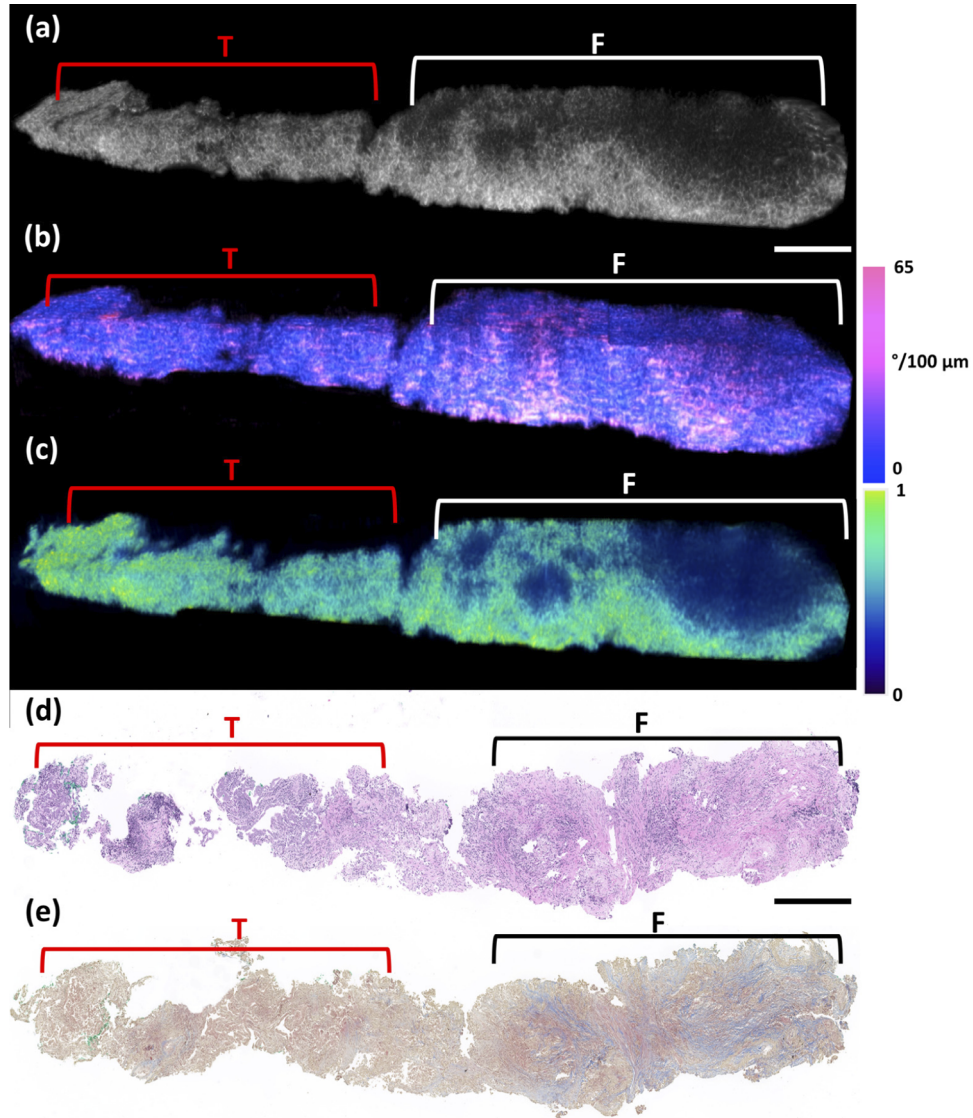


Fig. 4. Volumetric a) structural, (b) birefringence and (c) DOPU images oriented and cut obliquely for comparison with the histopathological features in the corresponding (c) H&E and (d) trichrome sections CNB specimen with adenocarcinoma in the left half and fibrosis in the right half of the specimen. Inflammatory infiltrates are present throughout the specimen. Birefringence colormap (b, right), ranging from 0°/100 μm (no birefringence) to 65°/100 μm (high birefringence). DOPU colormap (c, right), ranging from 0 (low DOPU) to 1 (high DOPU). Corresponding (d) H&E and (e) trichrome stained histology confirm the presence of tumor in the left half and fibrosis in the right half of the CNB specimen. Scalebars: 0.5 mm.

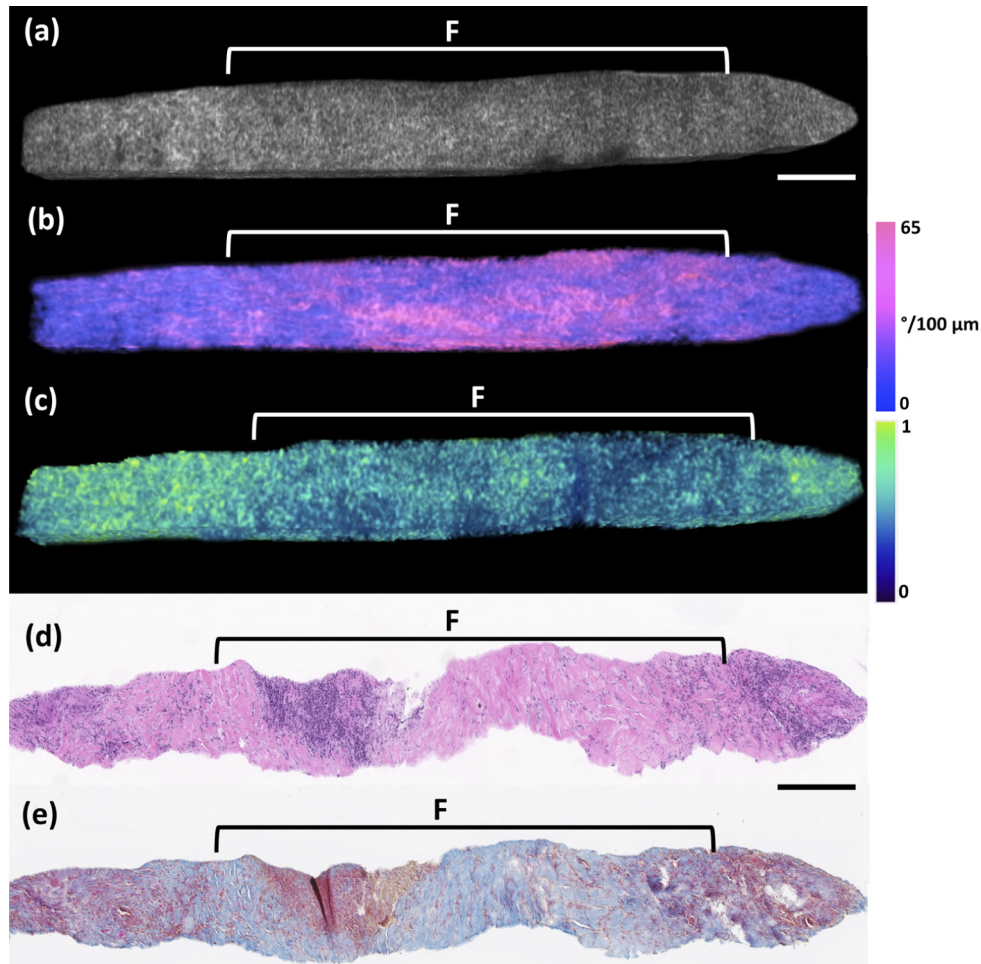


Fig. 5. Volumetric (a) structural, (b) birefringence and (c) DOPU images oriented and cut obliquely for comparison with the histopathological features in the corresponding (d) H&E and (e) trichrome sections of a CNB specimen consisting mostly of dense tumor associated fibrosis mixed with regions of inflammation. Birefringence colormap (b, right), ranging from $0^{\circ}/100\ \mu\text{m}$ (no birefringence) to $65^{\circ}/100\ \mu\text{m}$ (high birefringence). DOPU colormap (c, right), ranging from 0 (low DOPU) to 1 (high DOPU). Corresponding (d) H&E and (e) trichrome images, confirms the presence of dense tumor associated fibrosis, mixed with inflammation in the majority of the CNB specimen. Scalebars: 0.5 mm.

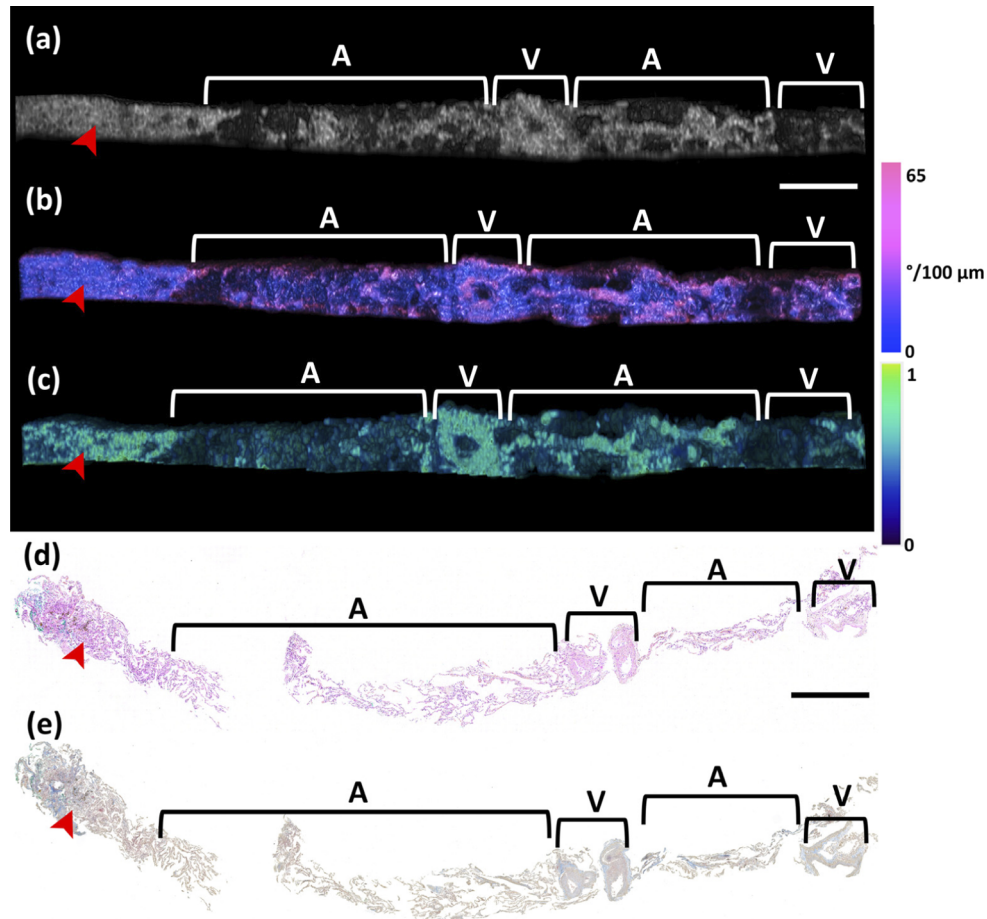


Fig. 6. Volumetric (a) structural, (b) birefringence and (c) DOPU images oriented and cut obliquely for comparison with the histopathological features in the corresponding H&E and trichrome sections of a CNB specimen consisting mostly of normal lung parenchyma, which appears as a lattice-like pattern of alveoli (A), with vessels (V). The region on the far left (red arrow) contains inflammation and pigment particles. Birefringence colormap (b, right), ranging from 0°/100 μm (no birefringence) to 65°/100 μm (high birefringence). DOPU colormap (c, right), ranging from 0 (low DOPU) to 1 (high DOPU). Corresponding (d) H&E and (e) trichrome images, confirming the presence of alveolar lung parenchyma, with small amounts of collagen within the alveolar walls and surrounding vessels. Scalebars: 0.5 mm.

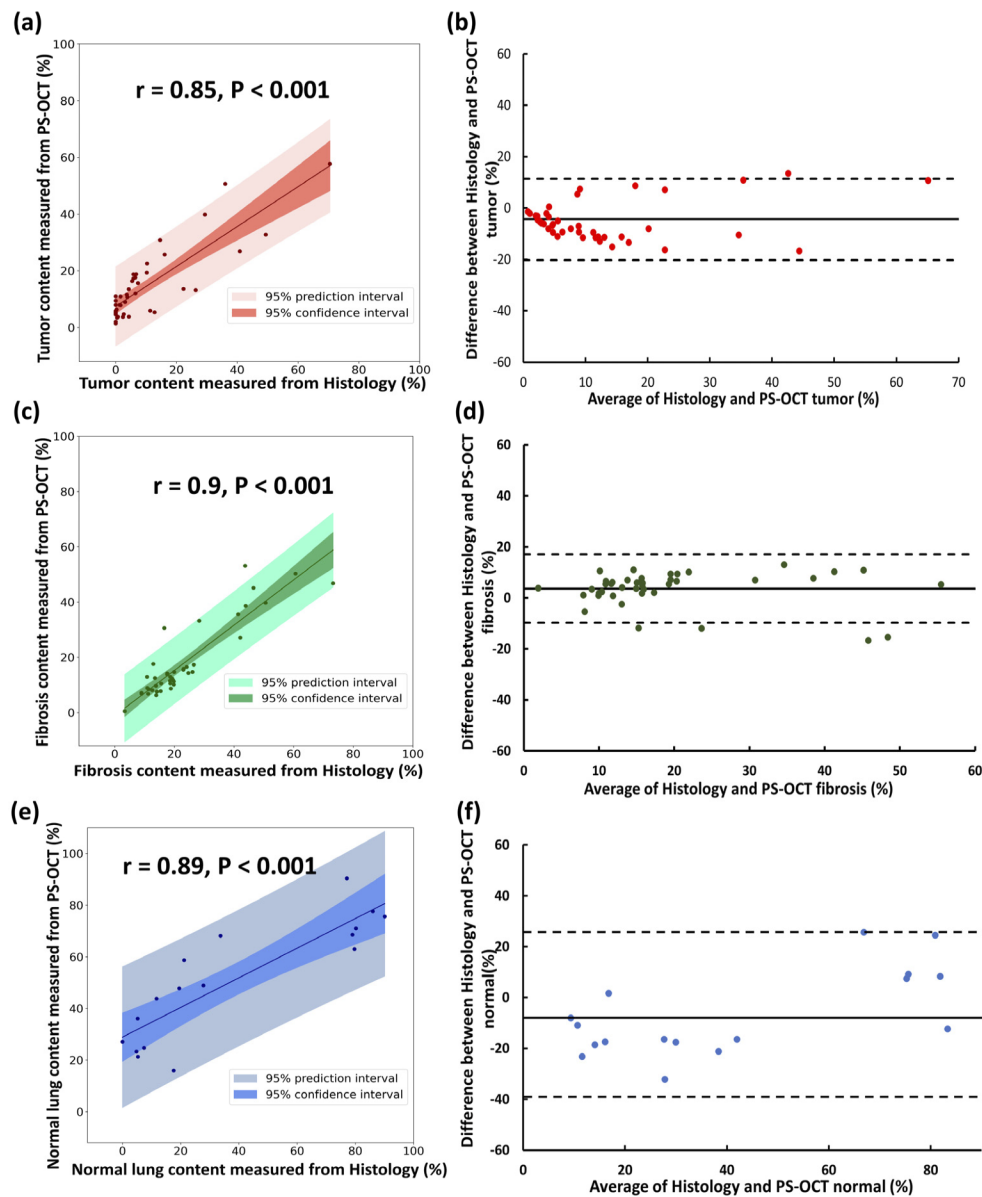


Fig. 7. Quantitative PS-OCT assessment of tumor, fibrosis, and normal lung components in CNB as compared to histology. **(a, c, e)** Linear regression analysis demonstrated strong correlation between PS-OCT and histology for quantifying **(a)** tumor ($r = 0.85$, $P < 0.001$), **(c)** fibrosis ($r = 0.9$, $P < 0.001$) and **(e)** normal lung parenchyma ($r = 0.89$, $P < 0.001$). The darker shaded bands in **(a, c, e)** indicate the 95% confidence intervals, whereas the lighter shaded bands indicate the 95% prediction intervals. **(b, d, f)** Bland-Altman analysis comparing PS-OCT and histology measurements showed an overall bias of **(b)** 5.61% for tumor, **(d)** -4.37% for fibrosis and **(f)** 6.58% for normal lung parenchyma, respectively. The dotted lines in **(b, d, f)** indicate the upper and lower 95% confidence intervals.

Table 2. Fisher's exact contingency table for classification of CNB specimens based on tumor and fibrosis content from PS-OCT versus histology.

Histology Quantification	PS-OCT Quantification			
	<i>Tumor</i>	$\leq 25\%$	$> 25\%$	Total
	$\leq 25\%$	34	2	36
	$> 25\%$	1	5	6
	Total	35	7	42
	<i>Fibrosis</i>	$\leq 25\%$	$> 25\%$	Total
	$\leq 25\%$	32	1	33
	$> 25\%$	1	8	9
	Total	33	9	42

4. Discussions

Adequate tumor sampling in CNB specimens is required for histologic diagnosis and molecular assessment of lung cancer, as well as for biobanking for future research. Ideally, transthoracic and transbronchial CNB procedures seek to obtain the highest possible tumor yield in CNB samples. However, a histopathology study examining the composition of biopsy samples reported that in biopsies containing $\leq 30\%$ tumor, 87.1% had some fibrosis present, and 41.6% had fibrosis as the most abundant tissue present in the biopsy [10]. This inadvertent biopsy of non-tumor elements hinders diagnosis and leads to repeat procedures. There is an urgent clinical need for a rapid, non-destructive method to assess adequacy of CNB specimens. In this study, we demonstrate the feasibility of PS-OCT for rapid, non-destructive, volumetric quantification and adequacy assessment of tumor, fibrosis, and lung parenchyma in fresh, intact lung CNB specimen with high sensitivity and specificity.

PS-OCT could allow physicians to rapidly evaluate CNB specimens intraprocedurally and assess whether they have obtained adequate tumor yield before ending the procedure, without freezing, labeling, or consuming any tissue. This would have significant potential to reduce the frequency of insufficient tumor yields on CNB specimens, which would reduce the need for repeat and/or more invasive procedures to acquire more tumor tissue. PS-OCT could also have major implications for tumor biobanking, both on CNB and surgical resection specimens, to maximize the amount of tumor preserved for future clinical and research needs. In order to have utility for rapid intraprocedural clinical use, CNB assessment must be attainable within clinically acceptable timeframes, without requiring complex interpretation skills from the user. In this study, PS-OCT image acquisition time was ~ 4 seconds and total processing time was ~ 4.3 minutes to generate structural, birefringence and DOPU volumetric image datasets for a CNB specimen, which is within a clinically acceptable timeframe. Conversion to a faster programming language and use of more powerful GPUs could also significantly enhance processing speeds. In contrast, frozen section analysis routinely performed for intraprocedural evaluation of surgical resection specimens takes ~ 20 minutes. The PS-OCT algorithm developed for CNB tissue quantification in this study was entirely automated, except for CNB total tissue region segmentation that was done manually. The implementation of a tissue surface identification algorithm would automate this step, and the entire processing and quantification process could be fully automated [35]. This would provide physicians with the means to perform rapid, intraprocedural assessment of tumor adequacy on volumetric CNB specimens without requiring training and expertise in PS-OCT image interpretation.

In addition to volumetric quantification of tumor content, PS-OCT has the added benefit of volumetric visualization of tumor and fibrosis distribution within CNB specimens, as demonstrated

in **Figs. 2–4**. Visualization of CNB content could have clinical utility for determining which CNB, or which part of a CNB, should be sent for specific diagnostic testing and/or research needs. This would be especially helpful in the setting of rapid molecular testing protocols, which aim to collect fresh CNB tissue and perform molecular testing in the fastest time possible to facilitate prompt therapeutic decision-making for patient care [36]. The densely packed collagen fibers in fibrotic regions appear highly birefringent; however, the regular variations of the adjacent polarization states in these regions can cause significant depolarization of light and lower the overall uniformity of polarization. In regions of tumor, the overall birefringence appears to be lower due to the lack of collagen, whereas polarization uniformity is preserved in these regions due to the modest attenuation and lack of multiple scattering of light, which may contribute to the higher DOPU. Normal lung parenchyma (**Fig. 5**) appears as thin, lattice like alveolar structure, that demonstrates low to moderate birefringence, which may be attributed to the presence of trace amounts of collagen in the alveolar walls, as seen on histology. The overall low signal intensity from the alveoli, and multiple scattering from the alveolar walls may contribute to lower DOPU values. These results are in agreement with prior studies investigating birefringence in lung and breast carcinoma that have demonstrated collagen-rich fibrotic stroma exhibits high birefringence while tumor regions lack substantial birefringence signal [24–26]. Our results are also in agreement with prior studies investigating DOPU in lung, breast, and cervical tissues, demonstrating that *in vivo* normal human lung, and fibrotic stroma in breast and cervical tissue had lower polarization uniformity due to scattering and significant variation in the polarization states resulting in lower DOPU, whereas tumor regions exhibited an overall uniformity of polarization states resulting in high DOPU [27–29].

There were several limitations in this study. Although PS-OCT measured volumetric tumor content correlated strongly with histological measurements ($r=0.85$), Bland-Altman analysis demonstrated that there was an overestimation bias of 5.61% in PS-OCT as compared to histology. The intercept of the correlation coefficient for the assessment of tumor quantification is greater than zero, suggesting that for biopsies with very little or no tumor, PS-OCT may overestimate the amount of tumor. Bland-Altman analysis also demonstrated an underestimation bias of -4.37% for fibrosis in PS-OCT as compared to histology. PS-OCT imaging was performed on fresh CNB specimens and compared against histology specimens after fixation and processing, which can cause considerable tissue shrinkage that may affect tissue type percentage quantification [37]. Because we are comparing quantification on volumetric PS-OCT imaging over the whole CNB sample against a single 2D histology slide, we cannot reliably determine whether the PS-OCT overestimation of tumor content is a false positive interpretation or is due to an issue with sampling error in the histology comparator. A more accurate, thorough comparison would require the use of 3D histology as the comparator, but this is a very time and labor-intensive process. Future studies using 3D histology will be needed to perform a more in-depth analysis comparing volumetric PS-OCT data against 3D histology in order to answer this question. In this study, we use a threshold value of < 25% tumor content being defined as ‘low tumor’, based on prior definitions of ‘low tumor’ reported in the literature. [33] The sensitivity and specificity at this threshold are high, with a low false positive rate. Future studies using 3D histology will be needed to accurately assess the sensitivity/specificity at lower threshold values for tumor content if required for clinical purposes.

It is also possible that additional elements may affect PS-OCT birefringence and DOPU measurements, which may have contributed to the overestimation and underestimation of tumor and fibrosis, respectively. Although DOPU has been used for assessment of various tissue types, such as breast, cervix, coronary plaque, wound healing, and retinal imaging, it has been shown that DOPU measurements are susceptible to system noise [38,39]. DOPU measurements may be also be affected by inflammatory infiltrates (**Figs. 2–4**), known to be variably associated with tumors, which could potentially contribute to overestimation of tumor on PS-OCT as compared to

histology. Environmental and smoking associated pigments are known to be present in variable amounts in the lung and combined with inflammation and/or fibrosis (**Fig. 5**), may also affect the DOPU measurement and alter classification. Blood vessels, consisting mostly of dense smooth muscle and trace amounts of collagen typically exhibit moderate birefringence, [31] and in **Fig. 5**, shows higher DOPU than the adjacent alveolar structures. When present, blood vessels may also affect classification. However, their distinctive circular, luminal structure (**Fig. 5**) may allow them to be distinguished from adjacent tissue. CNB specimens with storiform patterns of fibrosis may include small regions where the collagen fibers are oriented parallel to the incident OCT beam, and therefore, total collagen content will be under-estimated (**Figs. 2, 4**) [25]. In the current study, we have averaged the measurements of tumor, fibrosis, and normal lung across all the cross-sectional images in the OCT data volume for comparison with the corresponding regions labelled in the histology images. Despite these potential limitations, the combination of birefringence and DOPU metrics demonstrated strong correlation between PS-OCT and histology for quantification of tumor, fibrosis, and normal lung parenchyma. These results are also in agreement with prior studies investigating birefringence and DOPU in lung, breast, and cervical tissue [24–29]. Although the results are promising, this study should be considered a first step towards clinical translation. Larger studies, including studies with 3D histology, will need to be performed to validate and further explore the reported findings prior to clinical adoption. Future studies incorporating a more specific birefringence/DOPU ratio may improve the performance of the PS-OCT metrics to further differentiate malignant and benign tissues. Machine learning based algorithms may also be applied in future studies with larger sample sizes to assess whether this may improve the performance of PS-OCT based measurements for quantifying tumor in CNB specimens.

In this study, we focused on CNB tumor adequacy assessment in lung nodules. This was due to the clear clinical need for a rapid assessment method to increase tumor yield in order to meet histologic and molecular testing needs in lung carcinomas. However, similar rapid CNB assessment needs exist in other carcinomas, including breast and pancreatic carcinoma. Other studies have investigated PS-OCT for assessment of breast carcinoma [26,28]. It is expected that our findings would be translatable to tumor adequacy assessment in other organ systems, however, validation studies will need to be performed for further assessment. Needle-based OCT probes have been developed, which are compatible with bronchoscopy and would allow for PS-OCT imaging of tissues prior to CNB sample collection [26]. With the use of these probes, PS-OCT could be implemented *in vivo* to guide intraprocedural biopsy site selection by identifying and localizing potential biopsy sites with high tumor content while avoiding non-tumorous regions with fibrosis or atelectatic lung parenchyma. *In vivo* biopsy site assessment could be performed in conjunction with *ex vivo* CNB adequacy assessment to minimize the number of passes required and ensure adequate tumor yield in the obtained CNB specimens, respectively.

5. Conclusion

We demonstrate the feasibility of PS-OCT measurements to distinguish and quantify tumor, fibrosis, and normal parenchyma in fresh, intact lung CNB specimens. PS-OCT was able to classify CNB specimens with low tumor content ($\leq 25\%$) from high-tumor content ($> 25\%$) with high sensitivity and specificity, as compared to histology. The results indicate that PS-OCT has tremendous potential to maximize tumor yield for both clinical diagnostic and molecular testing purposes as well as for research biobanking. However, future, larger-scale studies will need to be performed to validate the findings of this study prior to clinical adoption.

Funding. National Heart, Lung, and Blood Institute (K23HL132120, R01HL152075); National Cancer Institute (R01CA167827); LUNGevity Foundation (2016-02).

Acknowledgments. We would like to thank Susan Sheng, PhD, from the Division of Pulmonary and Critical Care Medicine at Massachusetts General Hospital for helping with review and revision of the manuscript.

Disclosures. LPH: Boehringer Ingelheim, Pliant Therapeutics, LX Medical, and Biogen Idec. MJS: NinePoint Medical, LX Medical.

Data availability. Data underlying the results presented in this paper are not publicly available at this time but may be obtained from the authors upon reasonable request.

References

1. American Cancer Society, "Cancer facts & figures," American Cancer Society, Atlanta, Ga, USA, (2020).
2. National Lung Screening Trial Research Team, D. R. Aberle, A. M. Adams, C. D. Berg, W. C. Black, J. D. Clapp, R. M. Fagerstrom, I. F. Gareen, C. Gatsonis, P. M. Marcus, and J. D. Sicks, "Reduced lung-cancer mortality with low-dose computed tomographic screening," *N. Engl. J. Med.* **365**(5):395–409 (2011).
3. P. B. Bach, J. N. Mirkin, T. K. Oliver, C. G. Azzoli, D. A. Berry, O. W. Brawley, T. Byers, G. A. Colditz, M. K. Gould, J. R. Jett, and A. L. Sabichi, R. Smith-Bindman, D. E Wood, A. Qaseem, and F. C. Detterbeck, "Benefits and harms of CT screening for lung cancer: a systematic review," *JAMA* **307**(22), 2418–2429 (2012).
4. P. L. Shah, S. Singh, M. Bower, N. Livni, S. Padley, and A. G. Nicholson, "The role of transbronchial fine needle aspiration in an integrated care pathway for the assessment of patients with suspected lung cancer," *J. Thorac. Oncol.* **1**(4), 324–327 (2006).
5. M. P. Rivera and A. C. Mehta, "American College of Chest Physicians. Initial diagnosis of lung cancer: ACCP evidence-based clinical practice guidelines (2nd edition)," *Chest* **132**(3 Suppl), 131S–148S (2007).
6. J. S. Wang Memoli, P. J. Nietert, and G. A. Silvestri, "Meta-analysis of guided bronchoscopy for the evaluation of the pulmonary nodule," *Chest* **142**(2), 385–393 (2012).
7. L. Kim and M. S. Tsao, "Tumour tissue sampling for lung cancer management in the era of personalised therapy: what is good enough for molecular testing?" *Eur. Respir J.* **44**(4), 1011–1022 (2014).
8. F. J. Fintelmann, F. M. Troschel, M. W. Kuklinski, S. McDermott, M. Petranovic, S. R. Digumarthy, A. Sharma, A. S. Troschel, M. C. Price, L. P. Hariri, M. D. Gilman, J. O. Shepard, L. V. Sequist, and Z. Piotrowska, "Safety and Success of repeat lung needle biopsies in patients with epidermal growth factor receptor-mutant lung cancer," *The Oncol.* **24**(12), 1570–1576 (2019).
9. K. M. Kerr, "Personalized medicine for lung cancer: new challenges for pathology," *Histopathology* **60**(4), 531–546 (2012).
10. F. Goh, E. E. Duhig, B. E. Clarke, E. McCaul, L. Passmore, D. Courtney, M. Windsor, R. Naidoo, L. Franz, K. Parsonson, I. A. Yang, R. V. Bowman, and K. M. Fong, "Low tumour cell content in a lung tumour bank: implications for molecular characterisation," *Pathology* **49**(6), 611–617 (2017).
11. C. L. Coghlin, L. J. Smith, S. Bakar, K. N. Stewart, G. S. Devereux, M. C. Nicolson, and K. M. Kerr, "Quantitative analysis of tumor in bronchial biopsy specimens," *J. Thorac. Oncol.* **5**(4), 448–452 (2010).
12. G. da Cunha Santos, H. M. Ko, M. A. Saieg, and W. R. Geddie, "The petals and thorns" of ROSE (rapid on-site evaluation)," *Cancer Cytopathol.* **121**(1), 4–8 (2013).
13. M. Wang, H. Z. Kimbrell, A. B. Sholl, D. B. Tulman, K. N. Elfer, T. C. Schlichenmeyer, B. R. Lee, and M. Lacey, and J. Q. Brown, "High-Resolution Rapid Diagnostic Imaging of Whole Prostate Biopsies Using Video-Rate Fluorescence Structured Illumination Microscopy," *Cancer Res.* **75**(19), 4032–4041 (2015).
14. A. K. Glaser, N. P. Reder, Y. Chen, E. F. McCarty, C. Yin, L. Wei, Y. Wang, L. D. True, and J. Liu, "Light-sheet microscopy for slide-free non-destructive pathology of large clinical specimens," *Nat. Biomed. Eng.* **1**(7), 0084 (2017).
15. D. Huang and E. A. Swanson, C. P. Lin, J. S. Schuman, W. G. Stinson, W. Chang, M. R. Hee, T. Flotte, and K. Gregory, and C. A. Puliafito, "Optical coherence tomography," *Science* **254**(5035), 1178–1181 (1991).
16. S. H. Yun, G. J. Tearney, B. J. Vakoc, M. Shishkov, W. Y. Oh, A. E. Desjardins, M. J. Suter, R. C. Chan, J. A. Evans, I. K. Jang, N. S. Nishioka, J. F. de Boer, and B. E. Bouma, "Comprehensive volumetric optical microscopy in vivo," *Nat. Med.* **12**(12), 1429–1433 (2006).
17. G. J. Tearney, S. Waxman, M. Shishkov, B. J. Vakoc, M. J. Suter, M. I. Freilich, A. E. Desjardins, W. Y. Oh, L. A. Bartlett, M. Rosenberg, and B. E. Bouma, "Three-dimensional coronary artery microscopy by intracoronary optical frequency domain imaging," *JACC Cardiovasc Imaging* **1**(6), 752–761 (2008).
18. M. J. Suter, B. J. Vakoc, P. S. Yachimski, M. Shishkov, G. Y. Lauwers, M. Mino-Kenudson, B. E. Bouma, N. S. Nishioka, and G. J. Tearney, "Comprehensive microscopy of the esophagus in human patients with optical frequency domain imaging," *Gastrointest Endosc.* **68**(4), 745–753 (2008).
19. M. R. Hee, J. A. Izatt, E. A. Swanson, D. Huang, J. S. Schuman, C. P. Lin, C. A. Puliafito, and J. G. Fujimoto, "Optical coherence tomography of the human retina," *Arch Ophthalmol.* **113**(3), 325–332 (1995).
20. W. M. Allen, K. M. Kennedy, Q. Fang, L. Chin, A. Curatolo, L. Watts, R. Zilkens, S. L. Chin, B. F. Dessauvage, B. Latham, C. M. Saunders, and B. F. Kennedy, "Wide-field quantitative micro-elastography of human breast tissue," *Biomed. Opt. Express* **9**(3), 1082–1096 (2018).
21. K. M. Kennedy, R. Zilkens, W. M. Allen, K. Y. Foo, Q. Fang, L. Chin, R. W. Sanderson, J. Anstie, P. Wijesinghe, A. Curatolo, H. E. I. Tan, N. Morin, B. Kunjuraman, C. Yeomans, S. L. Chin, H. DeJong, K. Giles, B. F. Dessauvage, B. Latham, C. M. Saunders, and B. F. Kennedy, "Diagnostic accuracy of quantitative micro-elastography for margin assessment in breast-conserving surgery," *Cancer Res.* **80**(8), 1773–1783 (2020).
22. J. F. de Boer and T. E. Milner, "Review of polarization sensitive optical coherence tomography and Stokes vector determination," *J. Biomed. Opt.* **7**(3), 359–371 (2002).

23. J. F. de Boer, C. K. Hitzenberger, and Y. Yasuno, "Polarization sensitive optical coherence tomography - a review [Invited]," *Biomed. Opt. Express* **8**(3), 1838–1873 (2017).
24. L. P. Hariri, M. Villiger, M. B. Applegate, M. Mino-Kenudson, E. J. Mark, B. E. Bouma, and M. J. Suter, "Seeing beyond the bronchoscope to increase the diagnostic yield of bronchoscopic biopsy," *Am. J. Respir. Crit. Care Med.* **187**(2), 125–129 (2013).
25. L. P. Hariri, D. C. Adams, M. B. Applegate, A. J. Miller, B. W. Roop, M. Villiger, B. E. Bouma, and M. J. Suter, "Distinguishing tumor from associated fibrosis to increase diagnostic biopsy yield with polarization-sensitive optical coherence tomography," *Clin. Cancer Res.* **25**(17), 5242–5249 (2019).
26. M. Villiger, D. Lorenser, R. A. McLaughlin, B. C. Quirk, R. W. Kirk, B. E. Bouma, and D. D. Sampson, "Deep tissue volume imaging of birefringence through fibre-optic needle probes for the delineation of breast tumour," *Sci. Rep.* **6**(1), 28771 (2016).
27. F. Feroldi, J. Willemse, V. Davidoiu, M. G. O. Gräfe, D. J. van Iperen, A. W. M. Goorsenberg, J. T. Annema, J. M. A. Daniels, P. I. Bonta, and J. F. de Boer, "In vivo multifunctional optical coherence tomography at the periphery of the lungs," *Biomed. Opt. Express* **10**(6), 3070–3091 (2019).
28. J. Wang, Y. Xu, K. J. Mesa, F. A. South, E. J. Chaney, D. R. Spillman, R. Barkalifa, M. Marjanovic, P. S. Carney, A. M. Higham, Z. G. Liu, and S. A. Boppart, "Complementary use of polarization-sensitive and standard OCT metrics for enhanced intraoperative differentiation of breast cancer," *Biomed. Opt. Express* **9**(12), 6519–6528 (2018).
29. W. Li, B. F. Narice, D. O. Anumba, and S. J. Matcher, "Polarization-sensitive optical coherence tomography with a conical beam scan for the investigation of birefringence and collagen alignment in the human cervix," *Biomed. Opt. Express* **10**(8), 4190–4206 (2019).
30. L. P. Hariri, M. B. Applegate, M. Mino-Kenudson, E. J. Mark, B. E. Bouma, G. J. Tearney, and M. J. Suter, "Optical frequency domain imaging of ex vivo pulmonary resection specimens: obtaining one to one image to histopathology correlation," *J. Vis. Exp.* **71**, 3855 (2013).
31. D. C. Adams, L. P. Hariri, A. J. Miller, Y. Wang, J. L. Cho, M. Villiger, J. A. Holz, M. V. Szabari, D. L. Hamilos, R. Scott Harris, J. W. Griffith, B. E. Bouma, A. D. Luster, B. D. Medoff, and M. J. Suter, "Birefringence microscopy platform for assessing airway smooth muscle structure and function in vivo," *Sci. Transl. Med.* **8**(359), 359ra131 (2016).
32. M. Villiger, E. Z. Zhang, S. K. Nadkarni, W. Y. Oh, B. J. Vakoc, and B. E. Bouma, "Spectral binning for mitigation of polarization mode dispersion artifacts in catheter-based optical frequency domain imaging," *Opt. Express* **21**(14), 16353–16369 (2013).
33. K. V. Ferry-Galow, V. Datta, H. R. Makhlof, J. Wright, B. J. Wood, E. Levy, E. D. Pisano, A. L. Tam, S. I. Lee, U. Mahmood, L. V. Rubinstein, J. H. Doroshov, and A. P. Chen, "What can be done to improve research biopsy quality in oncology clinical trials?" *J. Oncol. Practice* **14**(11), e722–e728 (2018).
34. M. B. Amin, *American Joint Committee on Cancer and American Cancer Society AJCC Cancer Staging Manual*, 8th Ed. American Joint Committee on Cancer, Springer Chicago IL; (2017).
35. D. C. Adams, H. Pahlevaninezhad, M. V. Szabari, J. L. Cho, D. L. Hamilos, M. Kesimer, R. C. Boucher, A. D. Luster, B. D. Medoff, and M. J. Suter, "Automated segmentation and quantification of airway mucus with endobronchial optical coherence tomography," *Biomed. Opt. Express* **8**(10), 4729–4741 (2017).
36. P. K. Hsu, H. C. Huang, C. C. Hsieh, H. S. Hsu, Y. C. Wu, M. H. Huang, and W. H. Hsu, "Effect of formalin fixation on tumor size determination in stage I non-small cell lung cancer," *Ann. Thorac. Surg.* **84**(6), 1825–1829 (2007).
37. I. Dagogo-Jack, C. G. Azzolli, F. Fintelmann, M. Mino-Kenudson, A. F. Farago, J. F. Gainor, G. Jiang, Z. Piotrowska, R. S. Heist, I. T. Lennes, J. S. Temel, M. J. Mooradian, J. J. Lin, S. R. Digumarthy, J. M. Batten, H. Robinson, V. Nose, M. Rivera, V. Nardi, D. Dias-Santagata, L. P. Le, L. V. Sequist, M. Pitman, J. O. Shepard, A. T. Shaw, A. J. Iafrate, and J. K. Lennerz, "Clinical Utility of Rapid *EGFR* Genotyping in Advanced Lung Cancer," *JCO Precision Oncol.* **17**(2), 1–13 (2018).
38. S. Makita, Y. J. Hong, and M. Miura, & Y. Yasuno, "Degree of polarization uniformity with high noise immunity using polarization-sensitive optical coherence tomography," *Opt. Lett.* **39**(24), 6783 (2014).
39. P. A. Keahey, B. E. Bouma, and M. Villiger, "Automated noise estimation in polarization-sensitive optical coherence tomography," *Opt. Lett.* **45**(10), 2748–2751 (2020).